Chapter 6

High gain CDRA design using Higher Order Mode

6.1 Introduction

According to the detailed analysis of the fundamental $HEM_{11\delta}$ mode of a CDRA conducted in till the last chapter, it was found that this mode radiates with moderate gain ~ 5–6 dBi. In chapter 2, designs for gain enhancement such as incorporation of loading of additional structures such as cavity, short horns, DRA arrays, electromagnetic band-gap (EBG) structures and superstrates. The above methods pose serious design complexity and impose tight fabrication tolerances. In this juncture, the higher modes (HOMs) of the CDRA can be exploited for high gain operation. In chapter 4, the higher order $HEM_{21\delta}$ mode was investigated which failed to qualify as a useful radiating mode, as it gave boresight-null radiation with azimuthally asymmetric radiation pattern, and low gain < 4 dBi. To be comparable with the $HEM_{11\delta}$ mode, the selected HOM should give broadside radiation, gain >> 6 dBi, low cross-polarization and be easily excited with standard feed techniques. From the literature, it can be understood that the $HEM_{1mp+\delta}$ modes of a CDRA radiates in the broadside direction due to the horizontal magnetic dipole like near-field patterns. Hence in this chapter, the $HEM_{13\delta}$ mode (alternatively the HEM_{131} mode) which is the lowest of the $HEM_{13p+\delta}$ family ($p = 0, 1, 2...$) of a CDRA is investigated. A standard slot feed is selected to excite the $HEM_{13\delta}$ mode. Important design aspects of the DRA such as the resonant frequency, impedance matching, and far-field gain patterns are discussed, and experimentally verified.

6.2 Slot Excited CDRA

In chapters 3 and 4, the microstrip slot feed (aperture feed) was shown to excite the desired DRA mode with excellent modal purity. In addition, the slot feed is also capable of exciting multiple radiating modes of a CDRA with minimal design complexity [69]. Thus, in this chapter, the slot feed is chosen to excite a CDR as shown by the schematic diagram in Fig. 6.1, where the inset figure highlights the slot design.

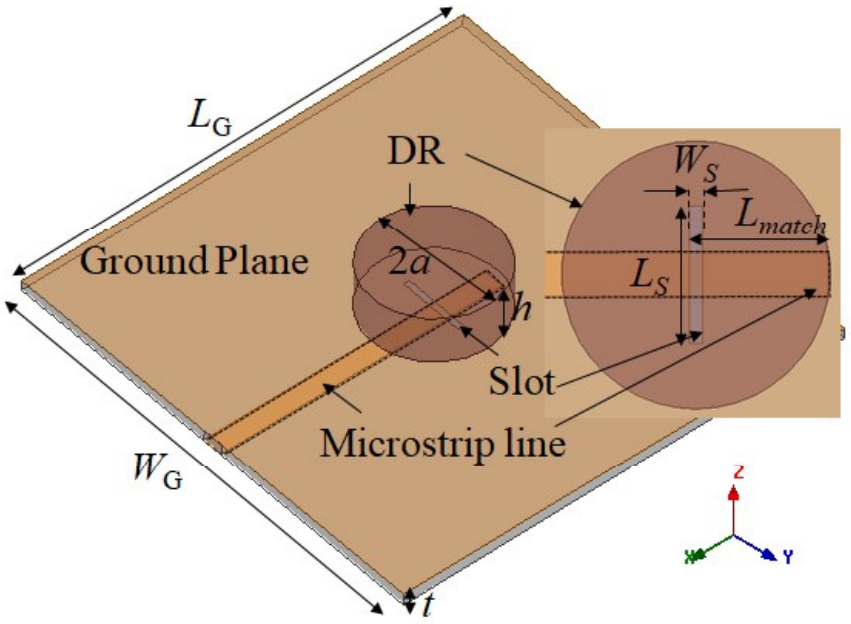

(a)

Fig. 6.1 Schematic diagram of the slot fed CDRA. (Substrate thickness (t) = 1.6 mm, substrate size (L_G or W_G) = 70 mm. substrate ε_r = 4 & tanδ = 0.02, slot size (L_S × W_S) = 10 mm×1 mm)

For a slot coupled CDRA, closed-form expression for the resonant frequency of the fundamental $HEM_{11\delta}$ mode, for $20 < \varepsilon_r < 24$ is given as follows [21],

$$f_0 = \frac{c}{2\pi a\sqrt{\varepsilon_r}}\left[1.71 + 2.0\left(\frac{a}{2h}\right) + 0.1578\left(\frac{a}{2h}\right)^2\right] \quad \ldots(6.1)$$

where c is the velocity of the light in vacuum and a/h is the aspect ratio of the CDR.

6.3 Parametric Analysis

6.3.1 Lower modes and Radiation pattern

Initial simulations use the properties of the available CDR (ε_r = 24, tanδ = 0.002, $2a$ = 19.43 mm, h = 7.3 mm and a/h = 1.33). For this CDRA, eq. (6.1) predicts a resonant frequency of 3.12 GHz. The slot feed is designed on a substrate of thickness (t) = 1.6 mm, side (L_G = W_G) = 70 mm, ε_r = 4 and tanδ = 0.02. The slot length L_s = 10 mm which is ~ $\lambda_g/3$, where λ_g is the effective wavelength in the CDRA [21]. The slot width W_s = 1 mm is chosen to be narrow enough so that it does not cause any spurious effects in the desired frequency range of the DRA

[70]. The microstrip line is designed for 50 Ω impedance. The impedance matching between the slot and the DRA is determined by the microstrip matching length indicated as L_{match} in Fig. 6.1. A parametric analysis of the CDRA model is initiated in ANSYS HFSS [28] by varying L_{match} and corresponding input reflection coefficient ($|\Gamma_{in}|$) versus frequency (2.5 GHz – 6.5 GHz) is shown in the Fig. 6.2.

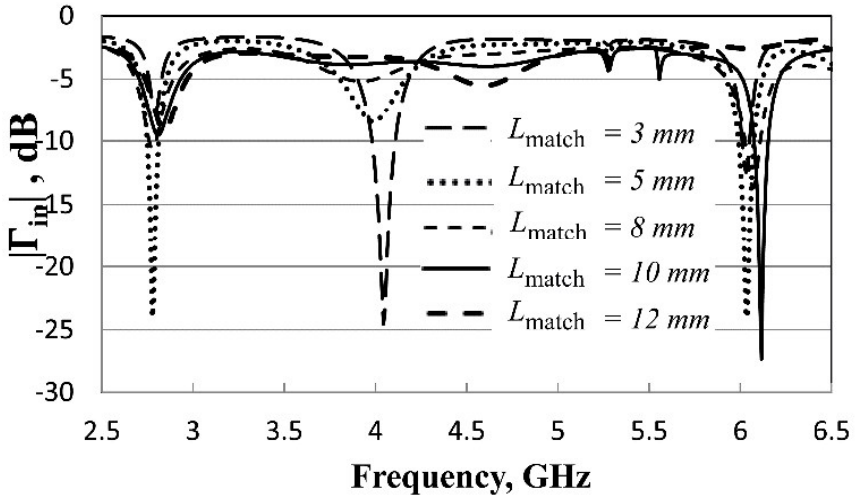

Fig. 6.2 Input reflection coefficient versus frequency for the first three mode of the slot fed CDRA as the function of L_{match}. (CDR : ε_r = 24, tanδ = 0.002, $2a$ = 19.43 mm and h = 7.3 mm)

In Fig. 6.2, three resonance dips corresponding to three DRA modes are observable, predominantly at around 2.8 GHz, 4 GHz and 6.1 GHz. Resonances above 6.5 GHz were found to produce either distorted radiation patterns or that with poor gain, hence are not explored further. The lowest resonance is obviously due to the $HEM_{11\delta}$ mode with resonant frequency of 2.78 GHz, which is about 12 % lower than that predicted by eq. (6.1). This error is attributed to the frequency detuning caused by the finite slot size [21]. An important observation that can be made from Fig. 6.2 is that the impedance matching of all the three resonances varies considerably with the matching length L_{match}. As seen, for L_{match} = 3 mm, the second mode is excited strongly; for L_{match} = 5 mm, the first and the third modes are excited strongly; for L_{match} = 10 mm, only the third mode is excited strongly, and for higher values of L_{match}, none of the

modes are excited strongly. This demonstrates a unique design feature of the slot feed of achieving mode selectivity simply by the proper selection of L_{match}.

The radiation patterns of the three modes, each with the best impedance matching design (L_{match} = 5 mm for the first mode, L_{match} = 3 mm for the second mode, and L_{match} = 10 mm for the third mode) are shown in Fig 6.3. It can be observed that all the three modes radiate in the broadside direction. Peak gains are 5.93 dBi at 2.78 GHz, 4.68 dBi at 4.045 GHz and 10.16 dBi at 6.116 GHz respectively for the first, the second and the third modes. It is interesting to note that the gain of the third mode is higher than that of the other two modes by at least 4 dB. It can also be noted that the cross-polarization level for any of the three modes is better than 25 dB, an advantage of using the slot feed [70].

To show how the peak gains of these modes vary with L_{match}, an appropriate graph is generated for all the three modes as shown by Fig. 6.4. In the figure, only those values of L_{match} giving $|\Gamma_{in}| < -10$ dB are considered. It can be confirmed from the figure that for any L_{match}, the third mode gives the highest gain. The maximum gain for the third mode occurs at L_{match} = 10 mm, which also ensures insufficient excitation of the lower two modes as observed in Fig. 6.2. As the focus of this work is on achieving high gain, further investigations are restricted to the third mode only. It was shown in chapter 5 that the ground plane size can control the quality (gain and cross-polarization) of the radiation pattern of the CDRA. So a suitable parametric study is conducted for the present DRA, and the ground size dependence of the peak gain and peak cross-polarization level for the third mode are plotted in Fig 6.5. As seen, at around L_G (or W_G) = 70 mm (~1.4 λ_0), the co-polar gain is a global maximum while the cross-polar gain is a global minimum, a trend that was followed by the $HEM_{11\delta}$ mode also.

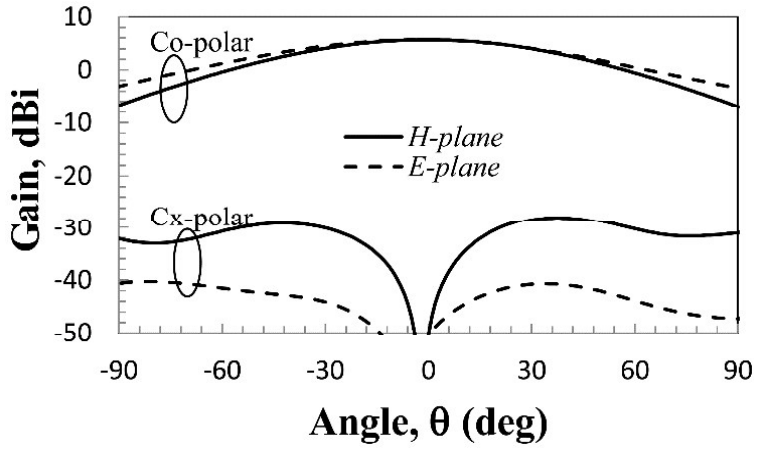

(a)

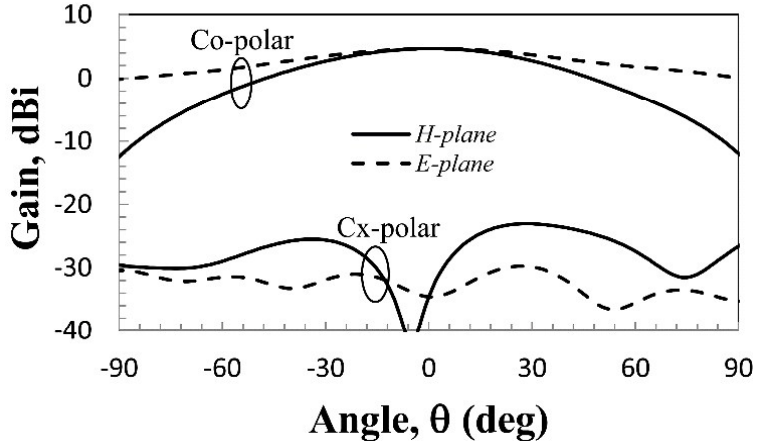

(b)

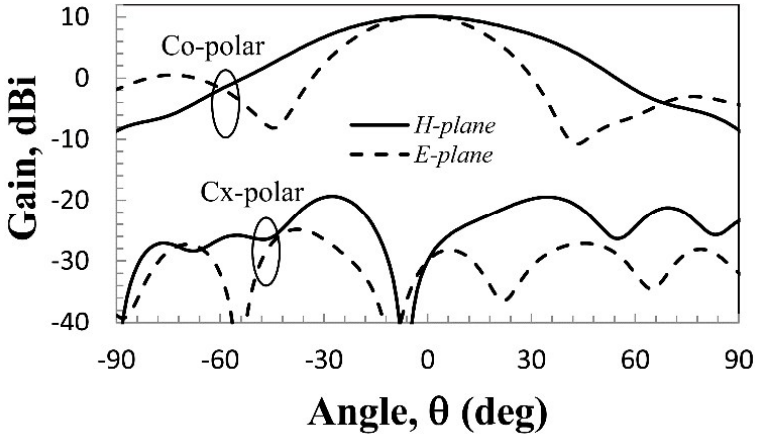

(c)

Fig. 6.3 Simulated radiation pattern of the slot fed CDRA (a) First mode at 2.78 GHz for L_{match} = 5 mm (b) Second mode at 4.045 GHz L_{match} = 3 mm (c) Third mode at 6.116 GHz L_{match} = 10 mm

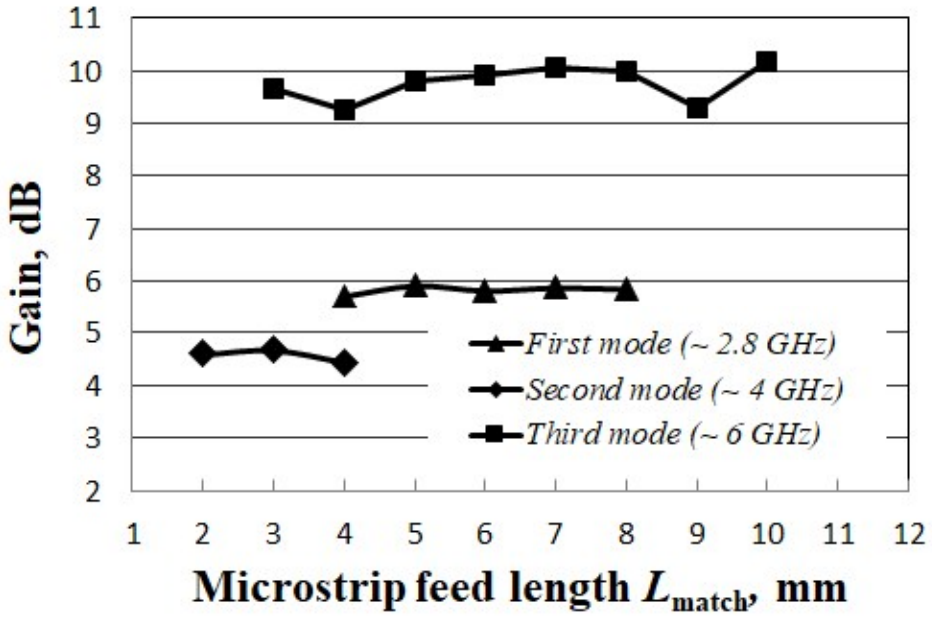

Fig. 6.4 Peak gains versus L_{match} for the three modes of the CDRA (CDR: ε_r = 24, tanδ = 0.002, $2a$ = 19.43 mm and h = 7.3 mm)

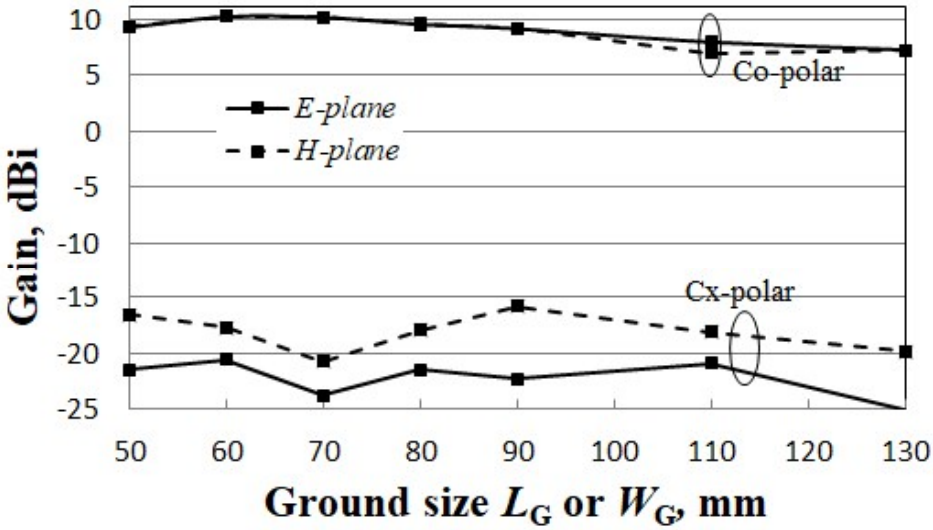

Fig. 6.5 Peak gain versus ground size for the third (high gain) mode for L_{match} = 10 mm (CDR: ε_r = 24, tanδ = 0.002, $2a$ = 19.43 mm and h = 7.3 mm)

6.3.2 Identification of the modes

Radiation patterns of the first two modes (Fig. 6.3(a & b)) share the common nature that the co-polar pattern in the *H*-plane is narrower, and the cross-polar level in the *H*-plane is higher, relative to the E-plane. The above features are typical to the $HEM_{11p+\delta}$ modal family that radiate like magnetic dipoles [55], [9], [21]. Next, the near-field pattern from HFSS of the first two modes are analyzed, and are shown in Fig. 6.6. Form the near-field plots it can be easily verified that the first resonance (~2.8 GHz) corresponds to the $HEM_{11\delta}$ mode. But the near-field analysis of the second resonance (~4 GHz) in Fig. 6.6(b) reveals that this mode even though appears like the $HEM_{11\delta}$ mode from the top view, is strongly perturbed by the slot field in the side view. So this mode may be called $HEM_{11\delta}$-like mode with resonant frequency given by that of the CDR-loaded-slot, $f_0 = \frac{c}{2L_s\sqrt{\varepsilon_{rav}}}$ = 4.01 GHz (where c is the light speed in vacuum, slot length L_s = 10 mm, $\varepsilon_{av} = (\varepsilon_{rDR} + \varepsilon_{rSUB})/2$ is the average dielectric constant between the CDR and the substrate). The calculated resonant frequency matches quite well with that simulated in HFSS (4.045 GHz). As the slot is an inefficient radiator compared to the DRA, the gain of this mode is lower than that of the fundamental $HEM_{11\delta}$ mode of the DRA.

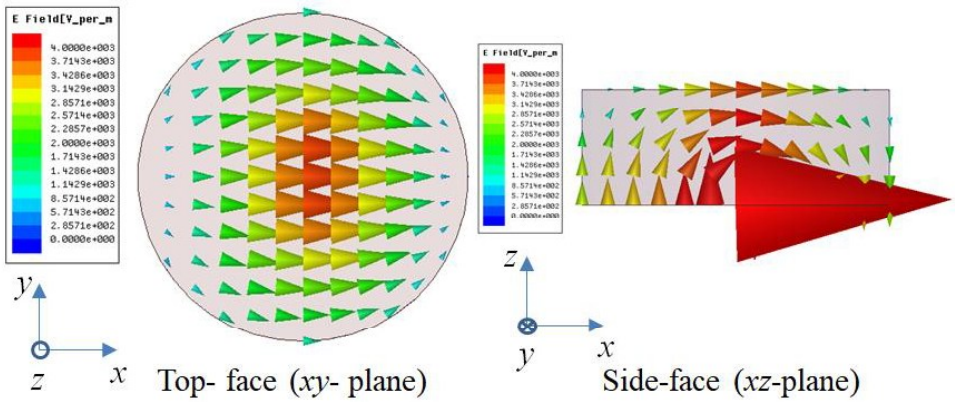

(a)

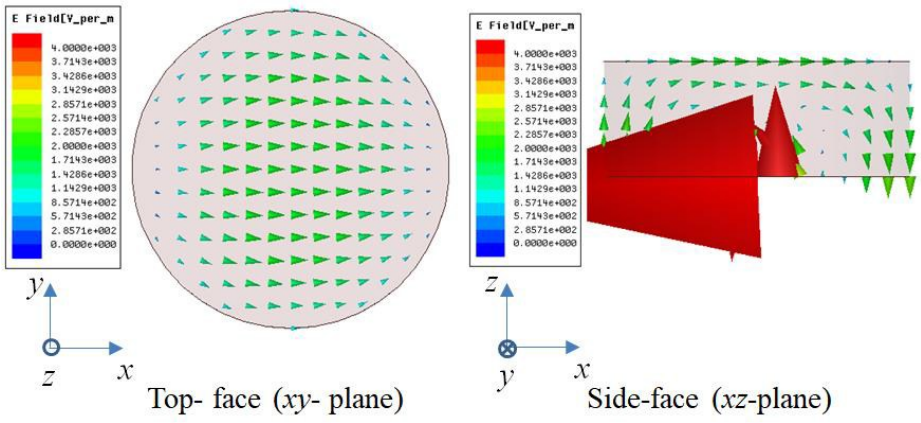

(b)

Fig 6.6. Near-field (Electric field) vector distributions (a) First mode at 2.78 GHz (b) Second mode at 4.045 GHz

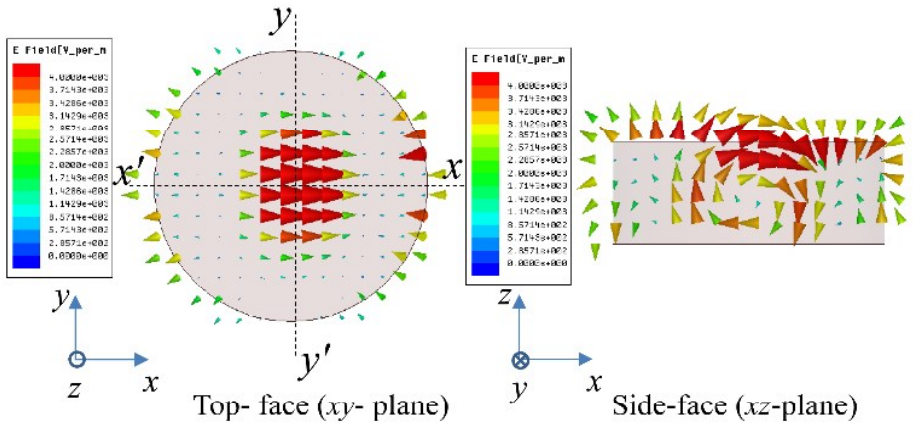

(a)

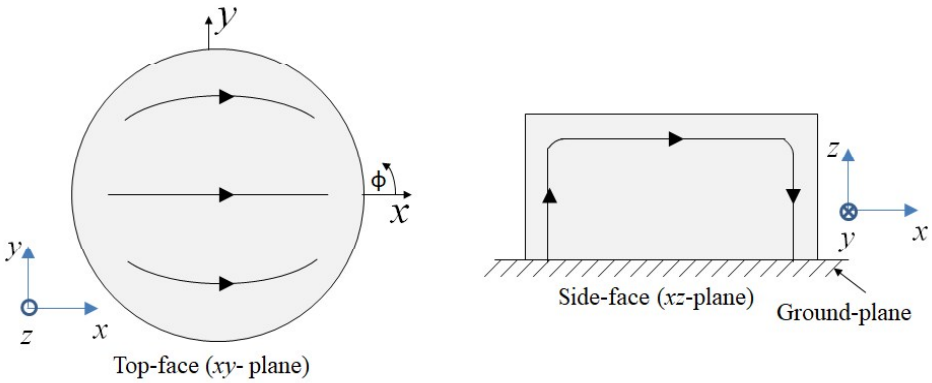

(i) $HEM_{11\delta}$

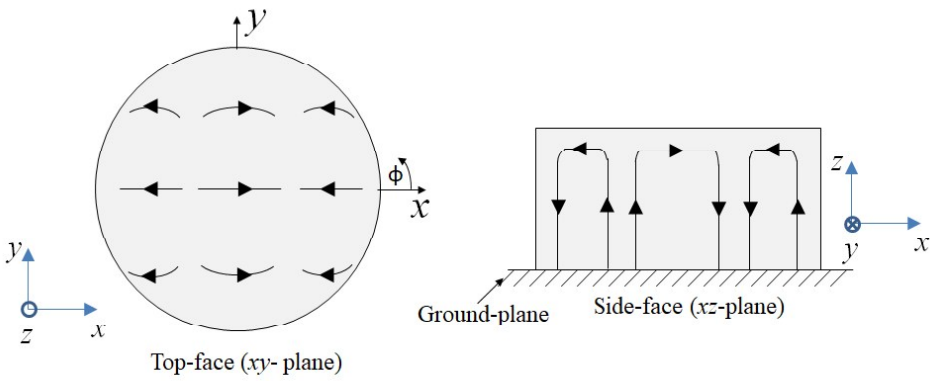

(ii) $HEM_{13\delta}$

(b)

Fig. 6.7 (a) Near-field vector distributions of the high gain ($HEM_{13\delta}$) mode at 6.116 GHz (CDR : ε_r = 24, tanδ = 0.002, $2a$ = 19.43 mm and h = 7.3 mm, L_{match} =10 mm, $L_G = W_G$ = 70 mm) (a) Electric (E) field from HFSS (b) Schematic illustrations of the electric field distribution of the (i) $HEM_{11\delta}$ mode (ii) $HEM_{13\delta}$ mode

However, through the proper optimization of the slot and the CDR parameters, the gain of this second mode may be improved for practical use. However, this aspect is not further considered here. Now the radiation of the high gain or the third mode (Fig. 6.3c) can be seen to exhibit some distinct features compared to the lower two modes such as (i) the patterns are more directional (ii) the pattern is broader in the H-plane than in the E-plane, and (iii) the E-plane pattern has two dips at around ±45 deg. These features imply a different modal family from that of the first two modes. For this mode (6.116 GHz), the near-field distributions in the DRA are as shown in the Fig. 6.7(a). Corresponding schematic illustrations are shown in Fig. 6.7(b) along with that of the well-known $HEM_{11\delta}$ mode. Two planes of the DRA are selected to analyze the field distributions – the top face (*xy*-plane) and the side face (*xz*-plane along *x*-*x*'). From the top face (Fig. 6.7(a)), the mode resembles some higher order $HEM_{11p+\delta}$ mode which is a contradiction to the inference drawn from the radiation pattern analysis. However, on the side face of Fig. 6.7(a), three λ/2 field variations (indicated by three full-loops) along the diameter are visible. Finally, as shown by Fig. 6.7(a) and (b), in the axial (*z*) direction, there is one λ/4

variation of the field (half-loop). Using the above-mentioned field variations, the high gain mode is named the $HEM_{13\delta}$ mode.

6.3.3 Effect of dielectric constant and aspect ratio of the CDR on the high gain mode

The dielectric constant (ε_r) and the aspect ratio (a/h) of the CDR are two major parameters that decide the resonant frequency, and to some extent the radiation pattern of DRAs. Hence a parametric study is initiated for the present DRA by keeping the diameter constant ($2a$ = 19.43 mm) and varying the ε_r and the a/h. In the initial simulation setup, the slot size is kept at 10 mm × 1 mm, the L_{match} at 10 mm and the ground size at 70 mm side. For each combination of ε_r and a/h, the peak gain of the first few resonances are calculated, and the mode with the maximum gain is identified through near-field analysis. Then through fine adjustments of the ground size and L_{match}, the impedance matching and the peak gain of the high gain mode are optimized. Corresponding resonant frequencies and gains are tabulated in Table 6.1.

For comparison, the ratio of the resonant frequencies of the high gain mode and the fundamental mode ($HEM_{11\delta}$) are also listed in the table. In Table 6.1, for DRAs with a/h = 1, the near-fields are found to be a combination of two or more modes, hence can't be identified correctly. Such modes are indicated in the table with the nomenclature of the closest resembling mode suffixed with 'like'. For example, the near-field distributions of two such cases is displayed in Fig. 6.8. For ε_r = 15, a/h = 1 (Fig. 6.8(a)), the mode is named as $HEM_{12\delta}$-like mode, and for ε_r = 35, a/h = 1 (Fig. 6.8(b)) it is $HEM_{11\delta}$-like mode. Further, it can be inferred from Table 6.1 that, CDRs with a/h > 1 favors the $HEM_{13\delta}$ mode, that resonates at about 2.2 times the resonant frequency of the $HEM_{11\delta}$ mode and exhibits a gain more than 8 dBi for any CDR under study.

The above aspects of the $HEM_{13\delta}$ mode, in combination with eq. (6.1) can be used for a rough estimate of the radiation performance of the mode. In the next section, the design giving the maximum gain of 10.16 dBi (ε_r = 24 and a/h = 1.3) will be experimentally verified.

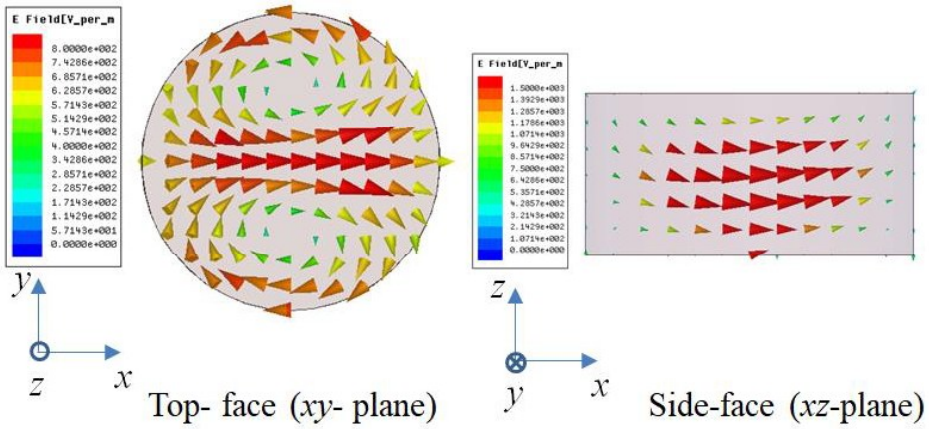

(a)

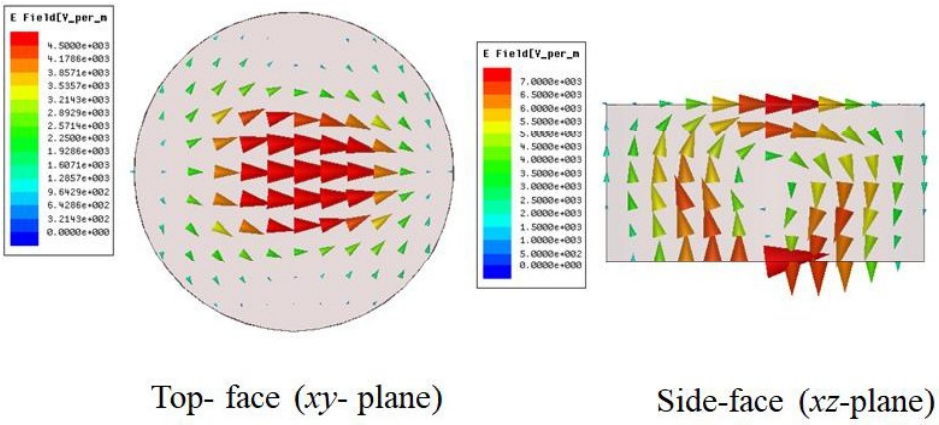

(b)

Fig. 6.8 Near-field distribution (E-field V/m) (a) For ε_r = 15, *a*/*h* = 1 (b) For ε_r = 35, *a*/*h* = 1 (referred to Table 6.1)

Table 6.1 Resonant frequencies and peak gains of the high gain mode of the CDRA for various dielectric constants (ε_r) and aspect ratios (a/h) of the CDR for $2a$ = 19.43 mm

CDR dielectric constant (ε_r)	Aspect ratio (a/h)	Resonant frequency of the high gain mode		Peak gain (dBi)	Mode nomenclature
		(GHz)	Relative to $HEM_{11\delta}$ frequency		
15	0.5	5.583	1.941	7.77	$HEM_{112+\delta}$
	0.7	5.141	1.710	8.13	$HEM_{111+\delta}$
	1	5.934	1.841	6.25	$HEM_{12\delta}$-like*
	1.3	7.541	2.210	9.12	$HEM_{13\delta}$
	1.5	7.918	2.244	9.49	$HEM_{13\delta}$
24	0.5	6.824	3.224	5.51	$HEM_{132+\delta}$
	0.7	6.107	2.523	9.78	$HEM_{112+\delta}$-like*
	1	5.332	2.085	7.59	$HEM_{13\delta}$-like*
	1.3	6.116	2.186	10.16	$HEM_{13\delta}$
	1.5	6.401	2.177	10.03	$HEM_{13\delta}$
35	0.5	6.248	3.224	7.52	$HEM_{114+\delta}$
	0.7	5.076	2.523	8.44	$HEM_{112+\delta}$-like*
	1	4.483	2.085	6.56	$HEM_{11\delta}$-like*
	1.3	5.055	2.186	9.07	$HEM_{13\delta}$
	1.5	5.244	2.177	8.21	$HEM_{13\delta}$

* These modes are difficult to identify, hence the term 'like' is used with them

6.4 Experimental Verification

Fabricated prototype of the CDRA (ε_r = 24, $2a$ = 19.43 mm, a/h = 1.33) is shown in Fig. 6.9. Measured and simulated reflection coefficients of the CDRA are compared in Fig. 6.10. Decent matching is observed between both the curves. In both simulation and measurement, the first mode is excited weakly at ~ 2.8 GHz, and the second mode at ~ 4 GHz is totally disappeared. The $HEM_{13\delta}$ mode is excited at 5.997 GHz with reflection coefficient $|\Gamma_{in}|$ = –18 dB in measurement. Corresponding resonant frequency and $|\Gamma_{in}|$ in simulation are 6.116 GHz and –28 dB respectively. The impedance bandwidths are 1.13 % and 1.28 % in measurement and simulation respectively.

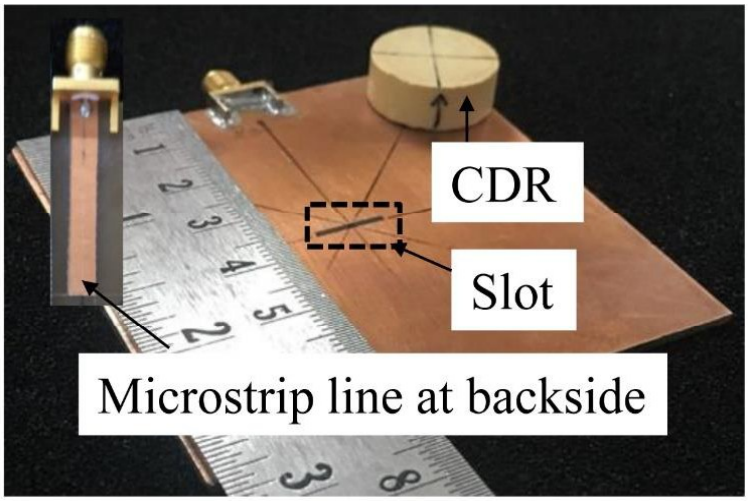

Fig. 6.9 Fabricated prototype of the slot fed CDRA (CDR : ε_r = 24, $2a$ = 19.43 mm, h = 7.3mm, tanδ = 0.002, Substrate : $L_G = W_G$ = 70 mm, t = 1.6 mm, ε_r = 4, tanδ = 0.02, Slot : L_S = 10 mm, W_S = 1 mm, L_{match} = 10 mm)

Measured radiation patterns in the two principal planes along with simulated patterns are shown in Fig. 6.11 which are in good agreement. Measured peak gain is 9.71 dBi which is close to the simulated peak gain of 10.16 dBi. The 3dB beam width in measurement and simulation are respectively 35^0 and 34^0 in the E-plane, while it is 68^0 and 67^0 respectively in the H-plane. The observed mismatches between the simulated and the measured results (Fig. 6.10 and Fig. 6.11) are caused by the fabrication and alignment errors of the slot fed DRA [7], and/or the errors in

the pattern measurement. The former error is responsible for the 10 dB difference between the simulated and the measured resonant dips (Fig. 6.10) which needs compensation.

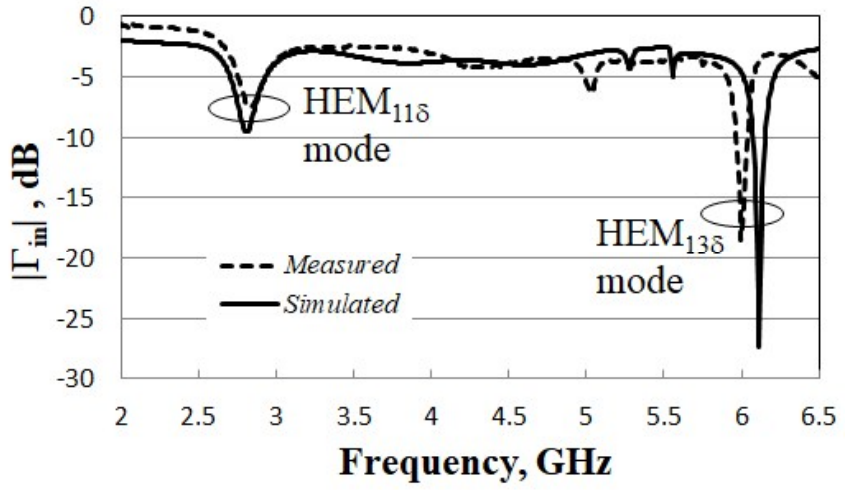

Fig. 6.10 Input reflection coefficient versus frequency for the slot fed CDRA (Fig. 6.9)

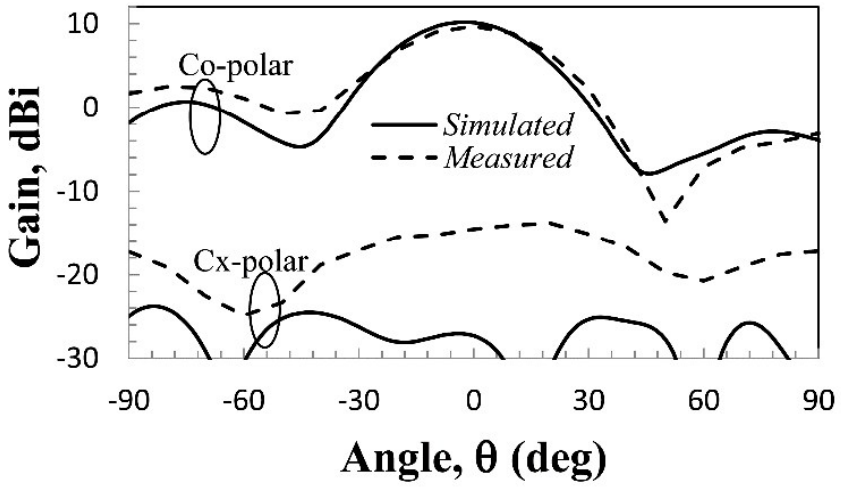

(a)

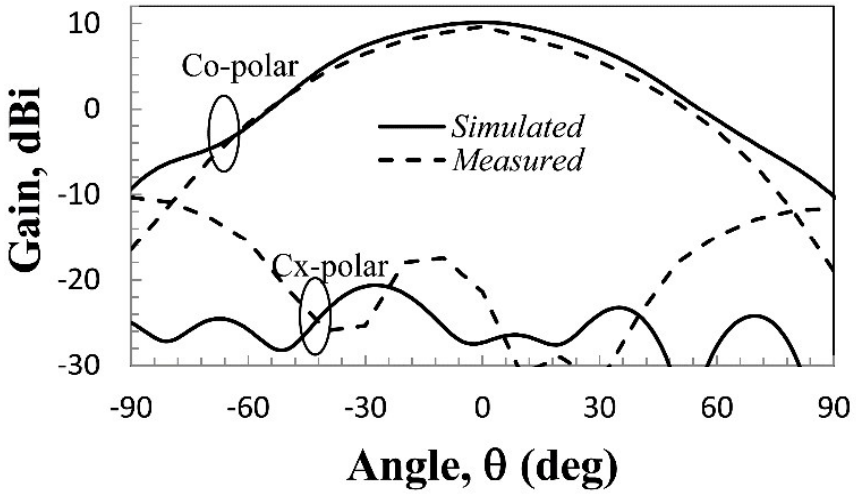

(b)

Fig. 6.11 Radiation patterns for the slot fed CDRA at 6.116 GHz (simulated) and 5.997 GHz (measured). (a) E-plane (b) H-plane

6.5 Improved Design for Impedance Matching

To improve the impedance matching of the DRA, a shunt stub is used with the microstrip line as done for the higher order $HEM_{12\delta}$ mode [35] as shown in Fig. 6.12.

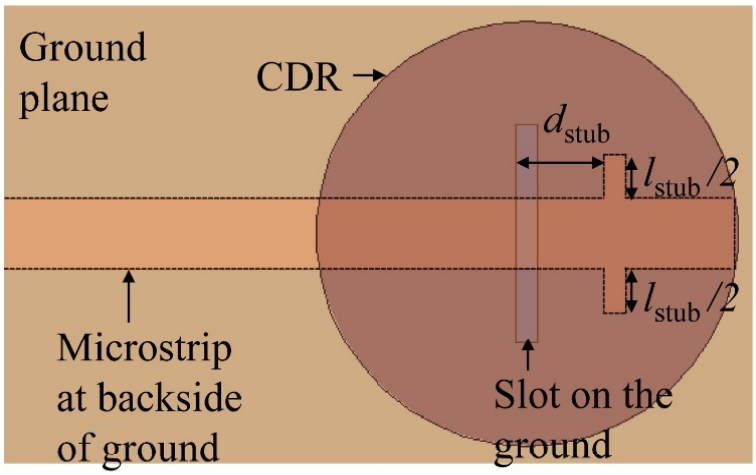

Fig. 6.12 Schematic representation of the improved slot fed CDRA with shunt stub matching (Other parameters as in Fig. 6.9)

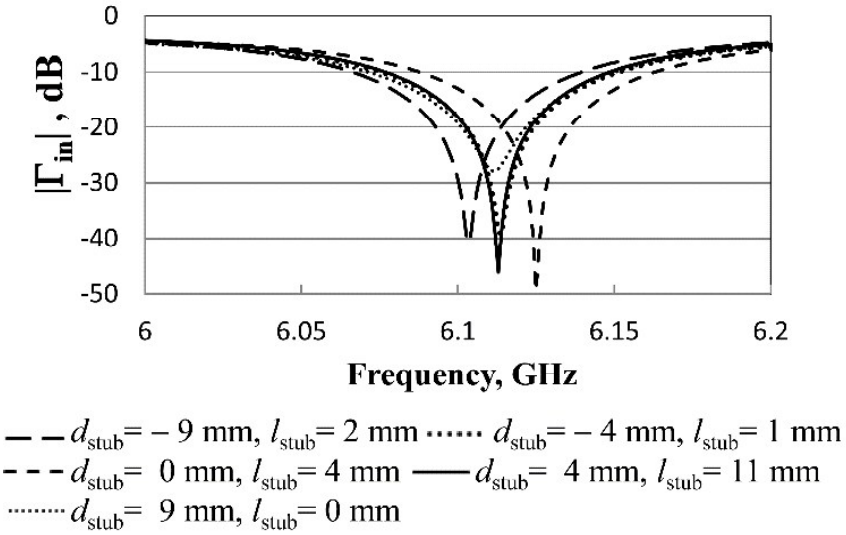

Fig. 6.13 Reflection coefficients of the slot fed CDRA for different stub location (d_{stub}) and stub length (l_{stub})

In the HFSS model of the present design, the stub width is kept the same as the slot width (W_S = 1 mm). And the stub length l_{stub} is optimized to attain the best impedance matching for a given stub position d_{stub} that is varied as d_{stub} = 0 mm, ±4 mm and ±9 mm with respect to the slot position. Here d_{stub} = 0 mm refers to the slot position while d_{stub} = 9 mm refers to the open end of the microstrip line. Corresponding variations in the reflection coefficients shown in Fig. 6.13 reveal that at d_{stub} = 0 mm and l_{stub} = 4 mm, the best impedance matching of $|\Gamma|_{min}$ = –49 dB is achieved. This imply ~21 dB better matching compared to that of the original CDRA (Fig. 10). The new resonant frequency is 6.125 GHz which is almost identical to the original frequency of 6.116 GHz.

6.6 Experimental Verification of the Improved Design

The fabricated model of the CDRA with stub loading is shown in Fig. 6.14 and the loaded stub as the inset. Measured reflection coefficient of the improved CDRA, relative to the original CDRA (Fig. 6.9) is shown in Fig. 6.15. In Fig. 6.15(a), the effect of stub loading is clearly visible that it mainly improves the reflection coefficient at resonance from –18 dB (at 5.997 GHz) to –32 dB (at 5.981 GHz). It is demonstrated in Fig. 6.15(b) that the stub loading has not affected the weakly excited $HEM_{11\delta}$ mode, owing to the selection of L_{match} = 10 mm for the

feed. Fig. 6.16 shows the principal plane radiation patterns of the CDRA for the original design and the improved design. As expected, the pattern shape and magnitude are preserved in the improved design. Table 6.2 compares the performance characteristics of the two CDRA designs which shows decent matching between each other. In addition, the simulated radiation efficiency is found as 71.85 % for the original design and 70.27 % for the improved design. In literature, the maximum gain achieved for a CDRA operated at a single HOM is 9.5 dBi at 7.5 GHz for the $HEM_{12\delta}$ mode [42]. In the above work, the $HEM_{12\delta}$ mode of a CDRA ($\varepsilon_r = 10$ and $a/h = 1$) is excited with a coaxial probe supported by a cavity loaded ground plane. The present design also demonstrates identical gain of 9.6 dBi (Table 6.2), but the cross-polar level of the present design is 6 dB lower compared to [42], by virtue of the slot excitation. Additional simulations predict that the gain of the present design can be improved by 1 dB and the radiation efficiency by 15 % with the use of high-quality substrate such as RT/duroid. Major drawback of the present design is the small impedance bandwidth due to the use of a high $\varepsilon_r = 24$ CDR [7]. However, by trading DRA gain for bandwidth [72] or by lowering the ε_r of the DR the bandwidth of the high gain mode may be increased. If the broadside gain enhancement over a wide band is the only concern irrespective of the mode, then dual-HOM operation of the DRA can be adopted [55], [7], [11].

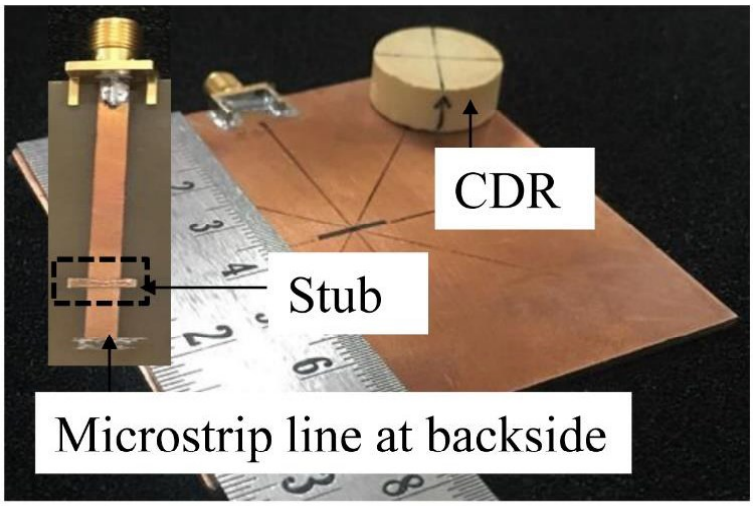

Fig. 6.14 Fabricated prototype of the simple slot fed CDRA (Stub : dstub = 0 mm, lstub = 4 mm, Other parameters as in Fig. 6.9)

Table 6.2 Performance comparison of the slot-fed CDRA without and with the stub for the $HEM_{13\delta}$ mode

Design		Resonant Freq., (GHz)	$\|\Gamma_{in}\|$ (dB)	Impedance bandwidth (%)	Peak gain (dBi)	Peak cx-pol level (dB)	Beam width E-plane (deg.)	Beam width H-plane (deg.)
Slot fed CDRA without stub	Simulated	6.116	–28	1.28	10.16	–30	35^0	68^0
	Measured	5.997	–18	1.13	9.71	–24	34^0	67^0
Slot fed CDRA with stub	Simulated	6.125	–49	1.23	10.14	–29	37^0	58^0
	Measured	5.981	–32	1.56	9.62	–21	36^0	52^0

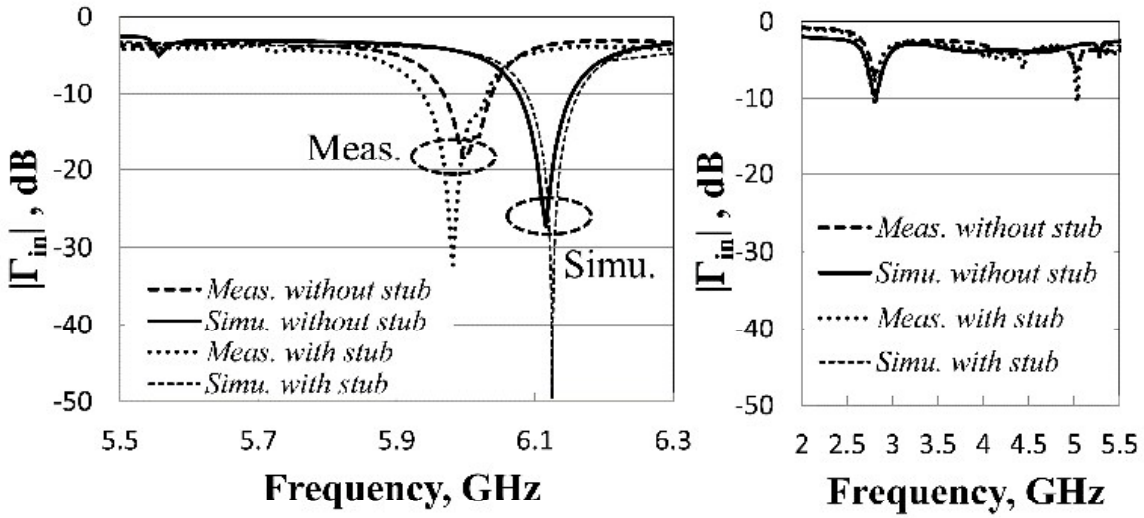

(a) (b)

Fig. 6.15 Measured versus simulated reflection coefficients of the slot fed CDRA (L_{match} = 10 mm, d_{stub} = 0 mm, l_{stub} = 4 mm) (a) Upper band showing only the $HEM_{13\delta}$ resonance (b) Lower band showing weakly excited $HEM_{11\delta}$ resonance

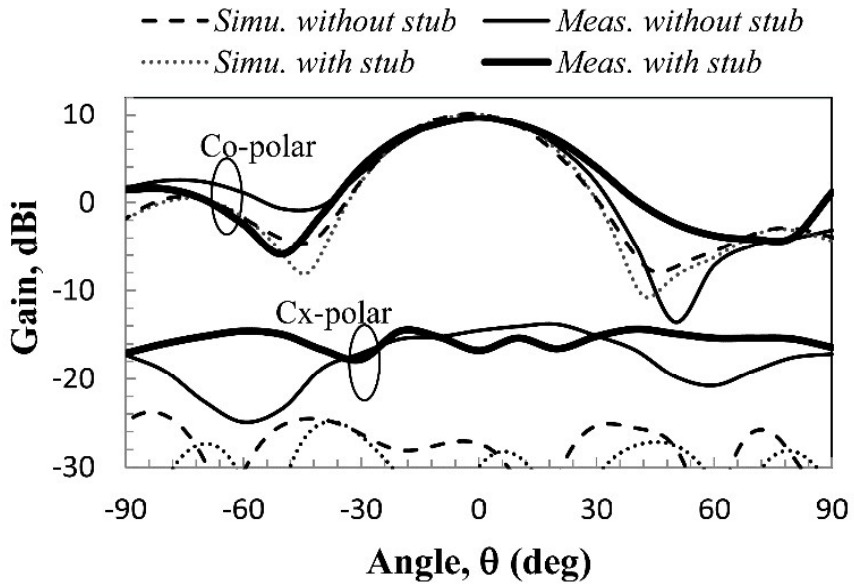

(a)

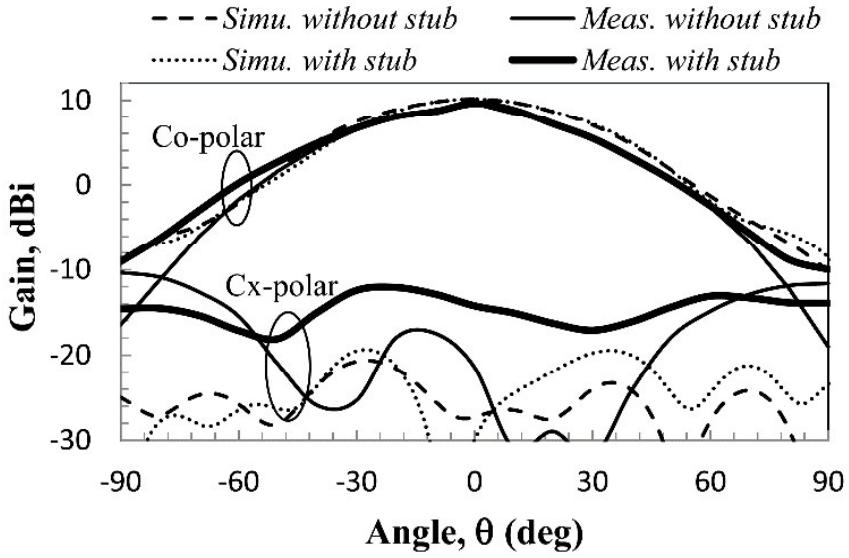

(b)

Fig. 6.16 Measured versus simulated radiation patterns of the slot fed CDRA. (a) E-plane (b) H-plane (Simulation: 6.116 GHz for without stub, 6.125 GHz for with stub, Measurement: 5.997 GHz for without stub, 5.981 GHz for with stub)

6.7 Conclusion

In this chapter, the $HEM_{13\delta}$ mode of a CDRA is demonstrated to be another useful broadside radiating mode of a CDRA similar to its predecessors the $HEM_{11\delta}$ and the $HEM_{12\delta}$ modes. However, like the $HEM_{12\delta}$ mode, $HEM_{13\delta}$ mode provides about 4 dB higher gain than the $HEM_{11\delta}$ mode. The major advantage of the present mode is that it can be excited with a simple slot feed providing additional advantage of lower cross-polarization, whereas the high gain $HEM_{12\delta}$ mode needs complex feed geometries. By loading a stub on the feed line, the reflection coefficient of the above mode is reduced by ~14 dB without notable variation in the other radiation characteristics. The $HEM_{13\delta}$ mode DRA may be a good choice for DRA arrays due to its high gain, low cross-polarization and ease of excitation.